DOI: 10.10 02/((please add manuscript number))
Article type: Article

Title: Intermediate-Phase Engineering via Dimethylammonium Cation Additive for Stable Perovskite Solar Cells

David P. McMeekin,[1,2,3§] Philippe Holzhey,[1§] Sebastian O. Fürer,[2,3] Steven P. Harvey,[4] Laura T. Schelhas,[5,6] James M. Ball,[1] Suhas Mahesh,[1] Seongrok Seo,[1] Nicholas Hawkins,[7] Jianfeng Lu,[2,3] Michael B. Johnston,[1] Joseph J. Berry,[4] Udo Bach[2,3]* and Henry J. Snaith[1]**

[1] Clarendon Laboratory, Department of Physics, University of Oxford, Parks Road, Oxford, OX1 3PU, United Kingdom

[2] Department of Chemical Engineering, Monash University, Victoria 3800, Australia

[3] ARC Centre of Excellence for Exciton Science, Monash University, Victoria 3800, Australia

[4] Material Science Center, National Renewable Energy Laboratory, Golden, CO 80401, USA

[5] Applied Energy Programs, SLAC National Accelerator Laboratory, Menlo Park, California 94025, USA

[6] Chemistry and Nanoscience Center, National Renewable Energy Laboratory, Golden, CO 80401, USA

[7] Department of Zoology, University of Oxford, South Parks Road, Oxford, OX1 3PS, UK

[§] These authors contributed equally to this work.

[*] Corresponding author E-mail: David.McMeekin@physics.ox.ac.uk

Udo.Bach@monash.edu, Henry.Snaith@physics.ox.ac.uk

Abstract: Achieving long-term stability of perovskite solar cells is arguably the most important challenge to overcome to enable widespread commercialization. Understanding the perovskite crystallization process and its direct impact on device stability is critical to achieve this goal. Surprisingly, we find that intermediate phases that occur during the crystallization process strongly influence the long-term perovskite device stability. The commonly employed "dimethyl formamide/dimethyl sulfoxide" (DMF/DMSO) solvent system preparation method results in poor crystal quality and microstructure of the polycrystalline perovskite films. In this work, we introduce a high-

temperature "DMSO-free" processing method that utilizes dimethylammonium chloride (DMACl) as an additive to accurately control the perovskite intermediate precursor phases. By precisely controlling the 2H to 3C perovskite phase crystallization sequence, we tune the grain size, texturing, orientation (corner-up vs face-up), and crystallinity of the formamidinium $(FA)_yCs_{1-y}Pb(I_xBr_{1-x})_3$ perovskite system. A population of encapsulated devices showed significantly improved operational stability, with a median T_{80} lifetime, for the steady-state PCE of 1190 hours and a champion device showed a T_{80} of 1410 hours, under simulated sunlight at 65 °C in air, under open-circuit conditions. Our work introduces an innovative processing method that allows higher overall perovskite device stability by controlling the intermediate phase domains during the perovskite formation. This work highlights the importance of material quality in order to achieve long-term operational stability of perovskite optoelectronic devices.

Introduction: With over 25% power conversion efficiencies (PCE),[1] organic-inorganic metal-halide perovskite solar cells have now reached a laboratory performance suitable for commercial applications. Although significant performance breakthroughs have been achieved since their humble beginnings, [2–12] their stability under operating conditions has yet to match state-of-the-art silicon-based solar cell technology. Recently, a number of research groups have demonstrated the ability of perovskite solar cells to pass a selection of tests from existing international electrotechnical commission (IEC) qualification standards for terrestrial PV modules such as the IEC 61215. However, this design qualification and test approval does not guarantee 25 years of operational stability. In particular, it is important to understand all types of degradations which may occur with this new solar absorber material in real-world use, which may not be tested for in IEC61215. [13–17] Significant advances have been made by mitigating thermal, structural, moisture, and light instabilities found in early perovskite compositions.

Moreover, these stability improvements have been enabled by enhanced encapsulation methods, ionic-liquid additives, Lewis acid-base passivation and by employing inherently more stable hole and electron accepting layers.[18–28]. Furthermore, a dramatic increase in thermal stability was achieved by replacing the volatile A-site cation, methylammonium ($CH_3NH_3^+$; MA), with a more thermally stable cation, formamidinium (($CH(NH_2)_2^+$; FA). Although neat $FAPbI_3$ forms in the desired cubic crystal structure at elevated temperatures (> 170 °C), once cooled to room temperature, it suffers from structural instability, where the black 1.47 eV photoactive corner-sharing 3D ABX_3 phase reverts to a yellow wide-bandgap face-sharing non-perovskite phase crystal structure. Hence, a second cation, notably caesium (Cs^+), is often used to facilitate structural stabilization of the black α-phase of FA-based perovskites without the use of the unstable MA cation.[29–34]

Finding the ideal ionic perovskite composition for long-term stability without compromising efficiency is an ongoing endeavour. In this work, we focus on an often-overlooked aspect of perovskite stability: crystalline quality rather than composition. In recent years, the metal-halide perovskite field has converged towards a simple and easy perovskite fabricating route, introduced by Jeon et al.,[35] consisting of a DMF/DMSO solvent system along with an "antisolvent" e.g. chlorobenzene, toluene, diethyl ether or anisole (C_6H_5Cl, C_7H_8, $(C_2H_5)_2O$; or $CH_3OC_6H_5$) step to quench the perovskite growth.[36] Although this method is unlikely to be industry-compatible, it allows for facile fabrication of laboratory-scale prototypes, while providing an acceptable level of film reproducibility and uniformity for various perovskite compositions. During the spin-coating process, the antisolvent step triggers rapid nucleation of the perovskite-DMSO complexes, forming a series of intermediate phases, and extracts a significant fraction of the original high boiling point solvents.[37] A subsequent annealing step provides the thermodynamic conditions allowing a 3D corner-sharing perovskite to fully form. However, these DMSO lead halide and perovskite complexes (e.g.

DMSO·PbX_2 and $(DMSO)_2$·PbX_2) may lead to residual DMSO solvent trapped within the film due to their strong molecular interaction with perovskite/PbX_2 and a high boiling point, and is just one of a whole range of possible precursor phase routes which could be explored, and may lead to higher quality perovskite.[38–41] The anti-solvent quenching approach promotes rapid heterogeneous nucleation with a high density of nucleation centres, leading to a short crystal growth period. This technique results in materials with relatively small grain sizes, polycrystalline films, and a relatively high density of structural and energetic disorder. These defects tend to result in a higher trap-state density and shorter carrier diffusion lengths compared to lengthier homogeneous nucleation and growth methods, such as single crystal growth techniques.[42–44] Lastly, smaller grain sizes result in an increase in grain boundaries, leading to a higher surface defects density. Structural defects located at the grain boundary have been linked to the promotion of moisture-induced degradation pathways.[45]Even though these films operate very well initially in photovoltaic devices, improving the crystal quality towards a "single-crystal-like" perovskite film should represent a step towards enhancing the long term stability of perovskite stability films and devices.

We have studied the precursor solution chemistry and its impact on photovoltaic performance.[46,47] We observed the formation of dimethylamine ($(CH_3)_2NH$) and formic acid (HCOOH) in the solution via the hydrolysis of dimethylformamide. For the inorganic perovskite $CsPbI_3$, we and others have identified that the presence of DMAI, following hydrolysis of DMF via the addition of HI, results in DMA^+ being incorporated into the "now hybrid" perovskite $DMA_xCs_{1-x}PbI_3$.[48,49] We have also observed that the colloidal chemistry of the $FA_yCs_{1-y}Pb(I_xBr_{1-x})_3$ precursor solution changes over time when hydrohalic acids are added to accelerate this decomposition reaction.[50,51] These hydrohalic acid additives vary the lead polyhalide colloids density in the precursor solution. We interpreted these results to indicate that these colloids composed of lead coordination compounds: $[PbX_3]^{1-}$, $[PbX_4]^{2-}$, $[PbX_5]^{3-}$,

$[PbX_6]^{4-}$ serve as nucleation centres which impact the crystallization kinetics of the perovskite formation resulting in a change in texture, grains sizes and defects density.[50,52] We showed that a precursor solution aged with hydrohalic acids additives, resulted in highly crystalline and oriented perovskite grains. However, this method had some downfalls, where an "under-aged" solution would lead to lower crystallinity, smaller grain sizes, and lower charge-carrier mobilities. In contrast an "over-aged" solution would suffer from poor perovskite coverage across the substrate.

Here, we identify that a key component of the "acid-aged" perovskite solutions is the dimethylamine generated from the decomposition of DMF. With this insight, we introduce a new controllable method of precursor phase engineering with the addition of dimethylammonium halide, and specifically dimethylammonium chloride ($(CH_3)_2NH_2Cl$; DMACl). By utilizing DMACl as a crystallization agent, we can gradually transition via the hexagonal face-sharing perovskite polytypes (2H, 4H, 6H) towards a 3C corner-sharing perovskite, resulting in highly crystalline and textured thin films with a "face-up" perovskite unit cell orientation. Finally, we study the impact of improved material quality on long-term stability for the formamidinium-caesium-based perovskite using three distinct fabrication methods: the state-of-the-art "DMF/DMSO" processing route, the "DMF/acid" processing route, and our new "DMF/DMACl" processing route. Our findings establish links between the details of fabrication methods, namely the ink formulation in concert with the detail of the processing route chosen to manipulate material quality and, ultimately device stability.

Results and discussion:

It has been shown that prolonged exposure to air and/or water degrades DMF to the secondary amine, dimethylamine, and formic acid.[46,53]

$$(CH_3)_2NC(O)H \rightleftharpoons (CH_3)_2NH + HCOOH$$

Furthermore, in the presence of strong acids, such as HI or HBr, this process is accelerated, where hydrohalic acids act as catalysts for this reaction. We performed a time-of-flight secondary ion mass spectrometry (TOF-SIMS) measurement and detected residual amounts of DMA^+ in the perovskite film after a 185 °C, 90 mins annealing step in an oven for a film prepared from a DMF precursor solution aged for 48h with hydrohalic acids additives (Supplementary Fig. 1). Hence, we confirm that these hydrohalic acids in water (HI 57 wt. % H_2O and/or HBr 48 wt. % H_2O) causes fast hydrolysis of DMF while simultaneously providing a source of halide, causing an unintended and uncontrolled addition of dimethylammonium halide salt $(CH_3)_2NH_2^+ X^-$ into the perovskite solution.

In Fig. 1, we show the impact of the hydrolysis reaction of dimethylformamide on the morphology, crystallographic properties and the stability of halide compositional segregation under illumination of the $FA_yCs_{1-y}Pb(I_xBr_{1-x})_3$ perovskite system. With the addition of hydrohalic acids, we observed a significant change in morphology and grain growths as observed in the X-ray diffraction line widths Fig 3F. We see a change in the morphology of the films with the domains/apparent grains observed in SEM changing in size from a few hundred nanometres to several microns (Fig. 1B) commensurate with the scattering measurements.[50] Furthermore, we study perovskite films based on a wide bandgap (1.7-1.8 eV) $FA_yCs_{1-y}Pb(I_xBr_{1-x})_3$ perovskite precursor, suitable for perovskite-on-silicon tandem solar cells[29,54,55] or as the front-cell in all-perovskite tandem cells.[56,57] In Figure 1F-G, we display wide-angle X-ray scattering (WAXS) measurements, where we observe that the control "DMF/DMSO" route results in concentric Debye–Scherrer rings indicative of polycrystalline thin films with a low degree of texture. On the other hand, we observed a significant variation in intensity across the Debye–Scherrer rings, for the "DMF/acid" route, indicative of a highly textured film. In Supplementary Fig. 2-4, we present the in-situ crystallization WAXS

measurements for both fabrication methods, plotting scattering intensity versus time, revealing that the DMF/acid films crystallize at a significantly slower rate compared to the DMF/DMSO films, even though they crystallize at a higher temperature (185 °C vs 100 °C).

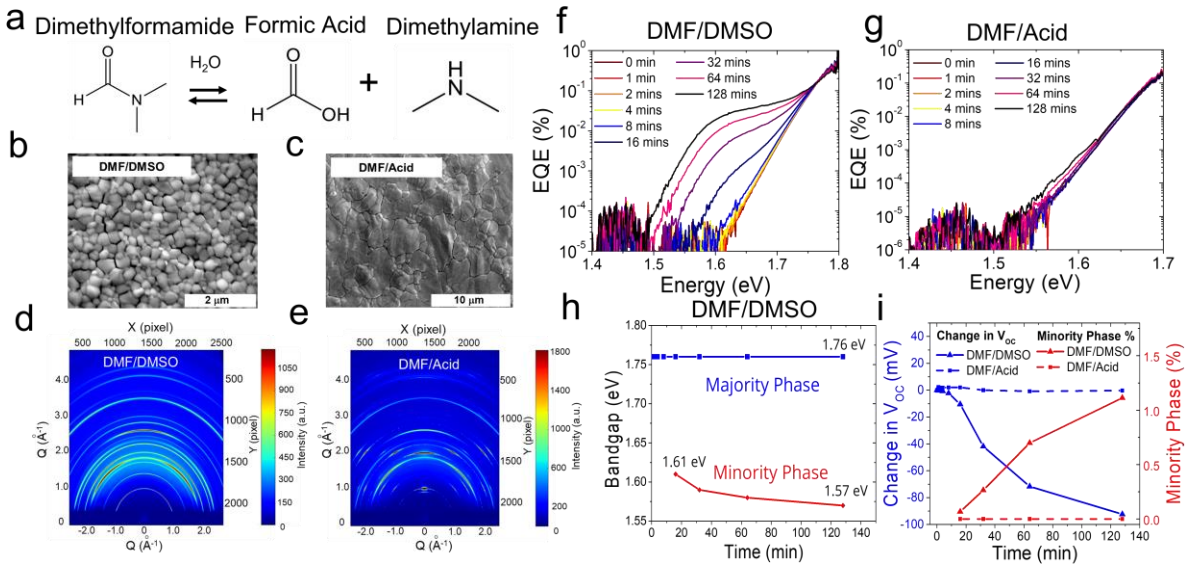

Figure 1: Impact of hydrohalic acids on the morphology, crystal quality and electronic disorder of the $FA_{0.83}Cs_{0.17}Pb(I_{0.6}Br_{0.4})_3$ perovskite film. A) Schematic showing the degradation of dimethylformamide (DMF) into dimethylamine and formic acid in the presence of water. The chemical equation of the DMF hydrolysis reaction, where DMF is the reactant, while dimethylamine and formic acid are the products. $(CH_3)_2NC(O)H \rightleftharpoons HCOOH + (CH_3)_2NH$. **B)** A scanning electron microscope (SEM) image of a $FA_{0.83}Cs_{0.17}Pb(I_{0.6}Br_{0.4})_3$ perovskite film prepared with a DMF/DMSO solvent mixture and **C)** with hydrohalic acid (HI/HBr) additives. **D, E)** Wide-angle X-ray scattering (WAXS) image of $FA_{0.83}Cs_{0.17}Pb(I_{0.6}Br_{0.4})_3$ perovskite films deposited on a fluorine doped tin oxide (FTO) substrate. **F, G)** External quantum efficiency (EQE), measured via Fourier transform photocurrent spectroscopy for a solar cell with a DMF/DMSO perovskite film and a DMF/acid perovskite film. For the EQE measurements, the devices were non-encapsulated and illuminated by a xenon-lamp simulated full-spectrum AM 1.5G, 100 mW cm^{-2} irradiance at open-circuit in air (humidity ~ 45 RH%) at room temperature. **H)** Quantification of the bandgap of the mixed-halide majority phase and the iodine-rich minority phase as a function of irradiation time, estimated from the EQE spectra shown in **I)**. Quantification of the V_{OC} loss due to the minority phase segregation, and the percentage of the minority phase as a function of irradiation time.

It is often observed that mixed-halide perovskite materials with high bromide content suffer from halide segregation,[58–61] where localized iodide- and bromide-rich perovskite domains form, when the films are exposed to light. Here, we performed external quantum efficiency (EQE) measurements, over a prolonged period of light exposure, of solar cells fabricated with perovskite films processed from these two different routes to assess the relative rate of halide segregation (Fig. 1e).[60] The steepness of the sub-bandgap absorption onset gives information about the electronic disorder in the absorber layer. This is often quantified as the exponential gradient, termed the Urbach energy. The pristine DMF/DMSO devices (i.e. at 0

min) have an Urbach energy of 16.0 meV, while the device with the DMF/acid perovskite showed a lower Urbach energy of 13.8 meV (Supplementary Fig. 5-6). Surprisingly, although the initial precursor salt composition was identical for DMF/DMSO and DMF/acid perovskite films, we found a strong time-dependence variation in electronic disorder between these two films. We follow our previously published approach in modelling the perovskite as being made of two components: a majority phase, and a phase segregated minority phase, which we describe in the SI.[60] We identify the majority phase as the bandgap of the material targeted for synthesis, while the minority phase is the low bandgap phase formed due to halide segregation, which occupies a volumetric fraction f of the film.

Through this analysis, we observed a sharp differential between $E_{g,majority}$ of 1.76 eV and $E_{g,minority}$ of 1.57 eV after 128 minutes of 1 sun illumination for the DMF/DMSO film. However, the DMF/acid films showed little to no variation in band gap over the same time period (Fig.3e). Lastly, Supplementary Fig. 7-11 shows the TOF-SIMS tomography of pristine and aged perovskite devices with the DMF/DMSO and DMF/acid perovskite films. The devices were aged under 1 sun illumination at maximum power point (MPP) for 24 hours. This measurement allowed us to assess the inhomogeneities of the FA/Cs A-site cations and the I/Br halides. After aging, we observed a stronger compositional variation for the DMF/DMSO perovskite films than the DMF/acid films, consistent with improved compositional stability of the DMF/Acid processed films.

From the measurements of the light-soaked devices, we estimated that the minority phase bandgap represents ~1.1% of the material after 120 minutes of illumination for the DMF/DMSO films, resulting in over 90 mV estimated loss in Voc. On the other hand, we observe only a slight increase in Urbach energy under illumination for the DMF/acid devices, but this increase remains well below the thermal energy, k_BT, where k_B is Boltzmann's constant and T is temperature. The absorption edge does not exhibit any discernible characteristic

shoulder, suggesting that compositional disorder increased only slightly; however, no distinct minority phase was formed. The corresponding open-circuit voltage loss due to this degree of segregation can be calculated to be less than 1 mV. As previously reported, we attribute this enhanced segregation stability to a higher level of ordering within the crystal lattice and/or larger grain sizes.[63] One possible hypothesis is that the improvement in crystal quality lowers the formation of native point defects such as vacancies (i.e. $V_{FA,Cs}$, V_{Pb}, and $V_{I,Br}$), interstitials (i.e. FA, Cs_i, Pb_i, and I, Br_i), and anti-site occupations (FA, Cs_{Pb}, FA_I, $Pb_{FA,Cs}$, $Pb_{I,Br}$, I, $Br_{FA,Cs}$, and I, Br_{Pb}) that can promote ionic motion within the perovskite crystal.[64] It has also been shown that the rate of halide segregation increases with increased non-radiative or trap-assisted recombination.[61,65,66] This may be due to the hole trapping process being responsible for liberating the mobile iodine diffusion which is a key part of halide segregation.

Intermediate, or precursor phases, commonly occur during the formation of polycrystalline metal-halide perovskite thin-films.[67] Although clearly influential, they are often an overlooked aspect of the complex crystallization process driven by thermodynamics. We observed that films prepared with a precursor solution aged with hydrohalic acids crystallized via distinct intermediate phases. We postulate that the source of these specific intermediate phases and thus control the formation process, is the unintentional presence of DMA^+. To test this theory, we prepared perovskite thin-films from precursor solutions which contained increasing concentrations of dimethylammonium halide salts (DMAX). Consistent with our hypothesis, we observed that this addition of the DMAX induces the formation of perovskite precursor phases, which allows for crystallisation to proceed via the formation of hexagonal perovskite polytype (2H, 4H and 6H) intermediate phases, which we illustrate in Fig. 2. This class of perovskite polytypes is comprised of a mixture of corner-sharing (cubic) and face-sharing (hexagonal) octahedral connections assembled in various ratios. This family of perovskites are commonly found in perovskite oxides, but have also been reported to occur

in metal-halide perovskites.[68–70] Here, we identify the $DMA_zFA_yCs_{1-y}Pb(I_xBr_{1-x})_3Cl_z$ perovskite system as part of this polymorphism class of material, where the proportion of cubic to hexagonal octahedral connections increases when exposed to high-temperatures (> 140 °C) (Supplementary Fig. 11); resulting in a phase transition from 2H to 4H to 6H face-sharing hexagonal frameworks, to eventually converge towards a fully 3C corner sharing cubic perovskite.[71]

As Mancini et al.[72] and García-Fernández et al.[73] have independently reported that $DMAPbX_3$, where X is I^-, Br^- or Cl^- anions, forms in various hexagonal face-sharing crystal arrangements. For example, $DMAPbI_3$ crystallizes in a 2H-hexagonal polytype with a space-group $P6_3/mmc$ comprising chains of face-sharing $[PbI_6]^{4-}$ octahedra separated by chains of DMA^+ cations,[74] whereas $DMAPbCl_3$ and $DMAPbBr_3$ both crystalize in a 4H-hexagonal perovskite polytype. These 4H perovskite polytypes are formed with Pb_2X_9 dimers of face-sharing octahedra, which are then connected to one another via corner-sharing octahedra.[73] Fig. 2 shows the intermediate phases occurring in the solvent-dried films, prior to the conversion to fully crystalline 3C perovskite form. After a 5 minute 100 °C anneal, we observe a colour change, along with the appearance of the 2H to 6H hexagonal polytypes phase, identified by X-ray reflections between $2\theta \sim 11.6° – 11.8°$. Moreover, we observe that with ≥ 20% excess DMACl (with respect to the Pb or combined FA + Cs content) we fully suppress the formation of the 3C cubic $FA_yCs_{1-y}Pb(I_xBr_{1-x})_3$ perovskite when heated at or below 100 °C. We assume that most of the solvent (DMF) has been removed from the film during this 100 °C annealing process, but most of the DMACl remains incorporated within the crystalline polymorphs. With a subsequent anneal at higher temperatures, we assume that most of the DMACl (the most volatile remaining component) is driven out of the film, until only the 3C cubic $FA_yCs_{1-y}Pb(I_xBr_{1-x})_3$ perovskite predominantly remains.

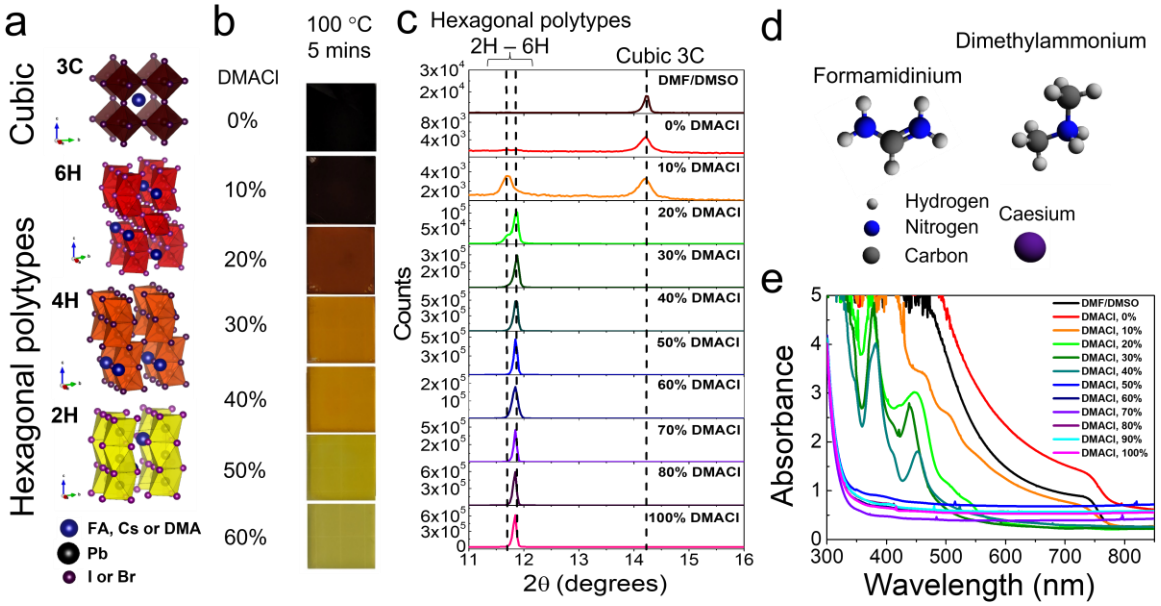

Figure 2: Impact of DMACl on the intermediate phases of the $FA_{0.83}Cs_{0.17}Pb(Br_{0.2}I_{0.8})_3$. A) *Crystal structure of a unit cell of the hexagonal lead halide perovskite polytypes: 2H, 4H, and 6H, showing PbI_6 octahedra connectivity along with a 3C cubic perovskite structure*. **B)** A series of photographs of $DMA_x(FA_{0.83}Cs_{0.17})_{1-x}Pb(Br_{0.2}I_{0.8})_3Cl_x$ perovskite films spin-coated with various amounts of DMACl additive, where percentages are expressed in excess amounts with respect to lead. **C)** A series of X-Ray diffraction patterns of the corresponding thin film showing the intermediate precursor phases in the form of hexagonal polytypes. **D)** A schematic of the A-site cations used in the perovskite crystallization process. **E)** Ultraviolet-visible (UV-Vis) absorbance spectra of corresponding thin films.

When adding DMACl in excess with respect to lead to the $FA_yCs_{1-y}Pb(I_xBr_{1-x})_3$ perovskite system, it appears to act as a "crystallizing agent" which controls the speed at which the 2H-4H-6H-3C crystallization sequence takes place. In turn, this directly impacts the nucleation dynamics, crystallization rate and final crystal quality of the 3C perovskite film. These hexagonal polytypes may template the perovskite orientation due to their similar hexagonal crystal structure to the 2H δ-$FAPbI_3$ "yellow" phase, which also exhibits a strong diffraction peak at 2θ ~11.8°. This offers a unique perovskite crystallization strategy, where the 2H to 3C crystallization sequence is controlled on a minute timeframe, rather than seconds for the standard DMF/DMSO solvent system. Furthermore, we highlight the fact that intermediate phases, induced with the additions of DMSO or DMAX, are indispensable for avoiding large macroscopic cracks, which are otherwise found in films processed from neat-DMF (Supplementary Fig. 12).

The intermediate phases induced by the $DMSO \cdot PbI_2$ and/or $(DMSO)_2 \cdot PbI_2$ complexes disappear within the first few seconds of the annealing process, leading to rapid crystal formation. For our DMF/DMACl route, we observe that little to no hexagonal face-sharing $DMAPbX_3$ crystal structure remains when DMAX is added in excess, and the films are annealed at elevated temperatures (> 185 °C) (Supplementary Fig. 13). Films with higher DMACl content do require longer annealing time or higher temperatures to fully remove the $DMAPbX_3$ crystal structure, which is consistent with the postulation that the excess DMACl needs to be volatilized from the film, for crystallisation to occur. We note that this is a similar requirement to when processing perovskite films from non-halide lead salts, such as lead acetate or lead chloride with an excess of A-halide cations.[75]

Eperon et al. have previously investigated substituting FA/Cs for DMA^+ in lead halide perovskites,[76] as opposed to the excess addition that we have undertaken here. To investigate the similarities and differences of these two approaches, in Supplementary Fig. 14, we show photographs, X-ray diffraction and ultraviolet-visible (UV-Vis) absorption data of a series of films that were prepared using a cation substitution method, where A-site FA/Cs cations were replaced by DMA^+ cations targeting a $DMA_y(FA_{0.83}Cs_{0.17})_{1-y}Pb(Br_xI_{1-x})_3$ perovskite system. Similarly to Eperon et al.,[76] we observed a slight blue shift in absorption onset when substitution the cation, however, this was accompanied by a lower preferred crystal orientation along the (100) plane. More importantly, we observe the presence of the formation of two separate phases, a 2H face-sharing located at $2\theta = 11.8°$ associated with δ-$FAPbI_3$ and/or $DMAPbI_3$, along with a 3C corner-sharing perovskite (Supplementary Fig. 14C and 16). We also observe a lowering of the steepness of optical absorption onset, indicative of an increase in electronic disorder.[77] Supplementary Fig. 17 shows films of the identical $DMA_y(FA_{0.83}Cs_{0.17})_{1-y}Pb(Br_xI_{1-x})_3$ perovskite system after a 185 °C annealing step. This high-temperature annealing step resulted in the removal of the 2H δ-$FAPbI_3$ and/or $DMAPbI_3$ peak;

however, significant PbX_2 peaks located at $2\theta \sim 12.7°$ appeared (Supplementary Fig. 17A and 15), presumably due to the sub stoichiometry of the FA and Cs cations in the starting solution. In contrast, when DMAX is added in excess amounts with respect to the $FA_{0.83}Cs_{0.17}Pb(Br_xI_{1-x})_3$, we obtain film morphology and crystal quality similar to the "acid method", where hydrohalic acids would hydrolyse the DMF over time to introduce DMA^+ into the precursor solution. This "excess cation" method is therefore different to the DMA^+ substitution explored previously and consists of a $DMA_y(FA_{0.83}Cs_{0.17})Pb(Br_xI_{1-x})_3X_y$, where X is I^-, Br^- or Cl^- anions, in a perovskite precursor solution, that serves to control the intermediate phases during the crystallization process. As shown in Supplementary Fig. 13, this results in highly textured perovskite films without any additional hexagonal polytypes remaining in the fully annealed films. Incidentally, if we add 50% excess $DMABr_xI_{1-x}$, as opposed to DMACl, we observed a 25 nm redshift in bandgap for films fully crystallised into the 3C perovskite, compared to neat $FA_{0.83}Cs_{0.17}Pb(Br_xI_{1-x})_3$ films, potentially due to a preferential loss of bromide (in DMABr) during the crystallization processing. Lastly, we have investigated the use of all DMAX cations and dimethylamine as an additive and have observed that all of these compounds can form hexagonal polytype intermediate phases (Supplementary Fig. 18-21). However, we found that in order to achieve an efficient device with a smooth perovskite morphology, DMACl was the most suitable additive, resulting in $DMA_x(FA_{0.83}Cs_{0.17})Pb(Br_{0.2}I_{0.8})_3Cl_x$ precursor phases. Notably, DMACl allowed for faster removal of excess compounds at lower temperatures, and did not significantly narrow the band gap of the perovskite, which is the case when adding DMAI/DMABr or HI/HBr in excess.

As reported by García-Fernández et al.,[74] due to the low dimensionality of the $DMAPbI_3$ crystal structure, this compound appears to behave as an ionic conductor but suffers from poor electronic conductivity. These insulating properties may be the reason why the optimum annealing requires high temperatures along with long durations in order to drive out

the face-sharing $DMAPbX_3$ perovskite. However, we note that a small portion of DMA^+ could potentially be incorporated into the cubic $(FA_{0.83}Cs_{0.17})Pb(Br_yI_{1-y})_3$ structure, as we measure some residual DMA^+ using time-of-flight secondary ion mass spectrometry (TOF-SIMS) (Supplementary Fig. 1). Ke et al. recently reported that up to 30% of the caesium in $CsPbI_3$ can be substituted with DMA^+, thus forming $Cs_{0.7}DMA_{0.3}PbI_3$ in a 3C corner-sharing cubic crystal structure.[48] Similarly, Marshall et al. recently showed that the $Cs_xDMA_{1-x}PbI_3$ perovskite only forms a pure-phase material with up to ≈ 25% DMA^+ substitution; above this point, the A-site cations begin to phase segregate.[49] Hence, assuming similar incorporation fractions, 4-5% (i.e. 25 to 30% of the 17% Cs) DMA^+ cations may be incorporated into the final perovskite structure. However, we did not observe a significant change in absorption onset between the "DMF/DMSO" and DMF/DMAX fabrication methods after fully annealing the neat iodide perovskite film at high temperature (Supplementary Fig. 21). For the remainder of the discussion, we will assume that there is only residual DMA^+ remaining in the final perovskite structure after crystallisation.

In Figure 3, we compare the crystallographic and photophysical properties of $FA_yCs_{1-y}Pb(I_xBr_{1-x})_3$ perovskite films prepared with the "DMF/DMSO" and the "DMF/DMACl" route. In Fig. 3D and Supplementary Fig. 22-24, we analysed the material quality using a two-dimensional (2D) X-Ray diffraction (XRD^2) system of a series of $DMA_z(FA_yCs_{1-y})Pb(Br_xI_{1-x})_3Cl_z$ perovskite films. We observed that the DMF/DMSO perovskite films showed (100) XRD peaks with azimuth angle (χ) located at approximately χ = ±25°, and films prepared with DMF solvent with 10% or less DMACl content resulted in (100) peak located at approximately χ = ±35°, corresponding to crystallites whose (100) planes are not completely perpendicular to the substrate, while the (101) plane becomes more perpendicular to the substrate upon DMA^+ addition, resulting in a "corner-up" perovskite film orientation. We note that these films tend to be highly polycrystalline with low levels of texture.

On the other hand, films with 20% or more DMACl had a strong (100) XRD peak located precisely at $\chi = 0°$, corresponding to crystallites whose (100) planes lie perpendicular to the substrate, thus producing a "face-up" orientation. These findings coincide with our previous XRD[2] analysis of the DMF/acid method, where films prepared with an aged solution with the addition of hydrohalic acids tend to orient their (100) peak to $\chi = 0°$.[50] Films with a high DMA^+ content have slower crystallization rates, allowing for "face-up" orientation to occur, while films with low or no DMA^+ content, such as the conventional DMF/DMSO films, crystallize at a much quicker rate, resulting in a significant portion of crystallite with a "corner-up" orientation. We hypothesize that crystallites may preferentially orient with their (100) plane parallel to the substrate if enough time and thermal energy is available. Similarly, Oesinghaus et al. established links between different $MAPbI_3$ perovskite fabrication methods prepared via various lead precursors (e.g. PbI_2, $PbCl_2$, or $Pb(CH_3COO)_2$) and their crystalline orientation.[78] Here, we expand on this knowledge by establishing links between the DMA-induced 2H-3C precursor phases, which govern the crystallization kinetics of the $FA_yCs_{1-y}Pb(I_xBr_{1-x})_3$ perovskite system in order to template the growth of the highly ordered "face-up" domains.

We studied the impact of DMACl on the morphology of the thin film and its crystallographic orientation, where DMACl is being used as a crystallizing agent to mimic the behaviour of hydrohalic acid addition. We show that the DMACl content controls the grain sizes and the crystallographic properties of the thin films. By allowing a much greater time span for the 2H to 3C sequence to occur, we observe that the perovskite crystal can orient itself with a significant (100) preferred orientation. As shown in Fig. 3C, by comparing XRD patterns of perovskite thin films with roughly identical thicknesses and scan parameters, we observe an increase of almost two orders of magnitude (77x) in the number of counts between the DMF processed neat $FA_{0.83}Cs_{0.17}Pb(Br_{0.2}I_{0.8})_3$ film and the $DMA_{0.5}(FA_{0.83}Cs_{0.17})Pb(Br_{0.2}I_{0.8})_3Cl_{0.5}$

processed film. Concurrently, we observe the disappearance of the XRD peak associated with the (110) orientation located at ~ 20.1° for precursor solutions with over 40% DMACl. Lastly, the full-width-half-maxima (FWHM) for the (100) peak was lowered by roughly a factor of two compared to the DMF/DMSO control, indicative of an increase in the crystal grain size and reduction in microstrain of the perovskite material (Fig 3F).

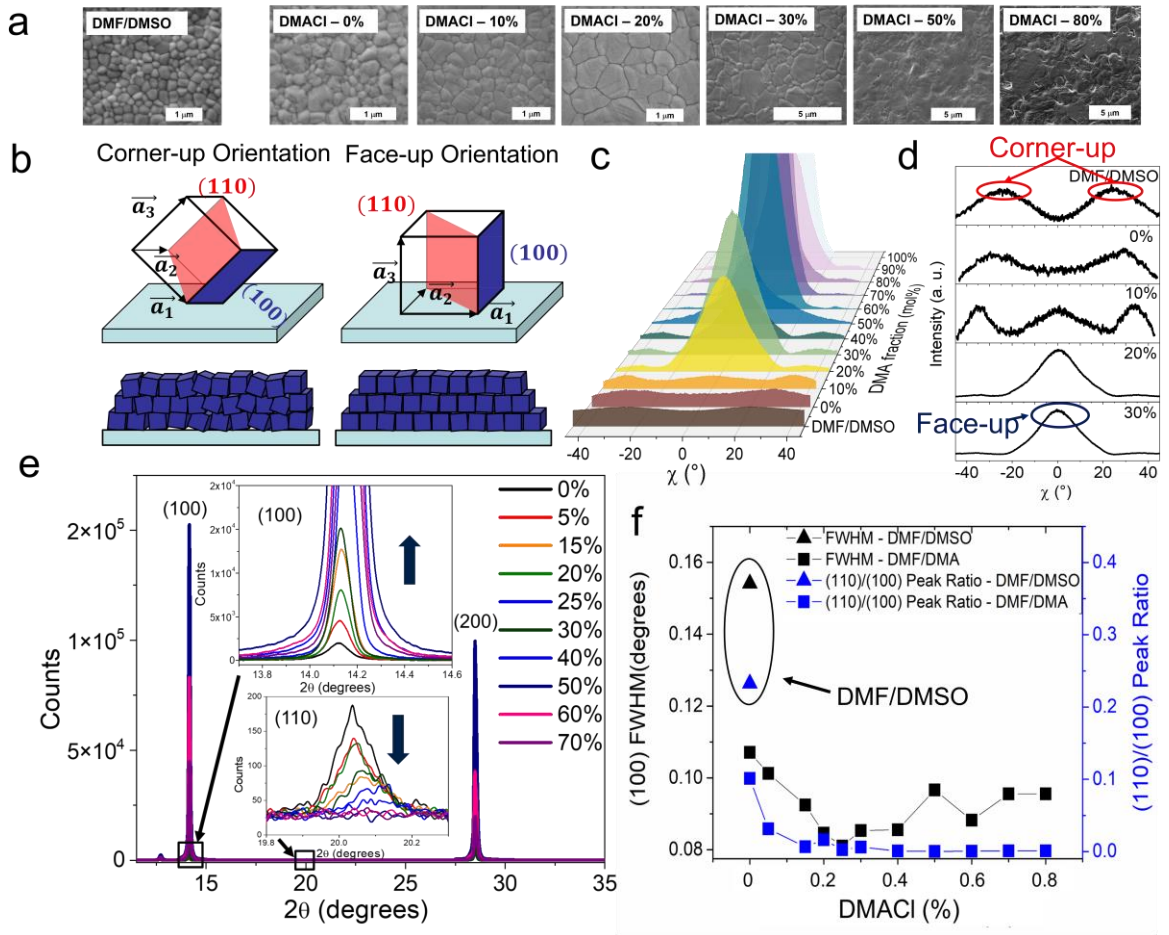

Figure 3: The impact of excess amounts of DMACl on the crystal quality, orientation and electronic disorder of the **$FA_yCs_{1-y}Pb(I_xBr_{1-x})_3$ perovskite** ***a)*** A series of scanning electron microscope (SEM) images and **b)** A schematic illustration comparison between the crystal structure with corner-up and face-up orientation with respect to the fluorinated-tin-oxide (FTO) substrate. **c)** A two-dimensional XRD beta peak analysis, showing the intensity (100) peak as a function of the azimuth angle (χ) for a series $DMA_x(FA_{0.83}Cs_{0.17})Pb(I_{0.8}Br_{0.2})_3Cl_x$ perovskite film. **d)** A series of two-dimensional XRD beta peak analyses of the (100) crystal plane for a series of $DMA_x(FA_{0.83}Cs_{0.17})Pb(I_{0.8}Br_{0.2})_3Cl_x$ perovskite showing a corner-up orientation for the DMF/DMSO films and the low DMACl content, while a face-up orientation is predominantly observed for films with 20% or more excess of DMACl **e)** One-dimensional X-ray diffraction (XRD) (Cu k-α) patterns of $DMA_x(FA_{0.83}Cs_{0.17})Pb(I_{0.8}Br_{0.2})_3Cl_x$ perovskite thin film with various amounts of excess DMACl after a full annealing step. **f)** A full-width at half maximum (FWHM) of the (100) XRD peak, measured with the 1D XRD, and a (110) to (100) XRD peak ratio for various DMA content films, compared to a DMF/DMSO solvent quenched film.

Now we proceed to investigate the impact of the different processing methodologies on the fundamental stability of the perovskite absorber layers. In Fig. 4, we show the impact of the perovskite processing solvent composition on the stability of perovskite thin films in a humid environment. A series of films prepared with various DMF to DMSO ratios were continually exposed to humid air with a relative humidity (RH) of approximately 85% at room temperature. We compared these films to our optimized highly orientated and crystalline DMF/DMACl processed $FA_{0.83}Cs_{0.17}Pb(I_{0.8}Br_{0.2})_3$ perovskite films. We observe improved stability with reducing DMSO content in the solvent and significantly improved stability for the DMF/DMACl processed films.

DMSO is a common Lewis-base solvent that is known to complex and coordinate with lead halide (PbX_2). This ability allows for intermediate precursor phases to occur and slow down the perovskite crystallization process and increase its "processing window".[37,79–81] However, the combination of strong molecular interaction with perovskite/PbX_2, along with a high boiling point, results in residual DMSO solvent remaining in the final perovskite film. Using nuclear magnetic resonance (NMR) spectroscopy, we analysed powders obtained from perovskite thin films that were dispersed in deuterated-acetonitrile (ACN-d3). By dispersing the perovskite powder in ACN-d3, residual DMF or DMSO solvent can be detected. Fig 4B shows residual solvent peaks for both DMF (7.93, 2.89 and 2.77 ppm)[82] and DMSO (2.51 ppm) for a thin film fabricated with a 50 μL drop-casted perovskite film, indicative that 1 hour 100 °C anneal is not sufficient to remove all solvents from a thick drop-casted film. Although a control DMF/DMSO solvent-quenched approach with ~ 500 nm thick films did not show any residual DMF, a DMSO peak could still be detected after the standard 1 hour 100 °C annealing step. On the other hand, the DMF-only perovskite film prepared with excess amount of DMACl is compatible with high-temperature annealing processing (> 170 °C), enabling the film to drive out any residual solvent from the films, while the 2H to 3C crystallization sequence takes place.

We note that DMACl allows for high-temperature processing without significant degradation of the $FA_{0.83}Cs_{0.17}Pb(I_{0.8}Br_{0.2})_3$ film (i.e. no significant PbX_2 XRD peak appears for temperatures below 200 °C for 7 minutes, as shown in Supplementary Fig. 25. We suspect that the entrapped solvent and low degree of texturing is the cause for the reduced humidity stability of the DMF/DMSO processed films.

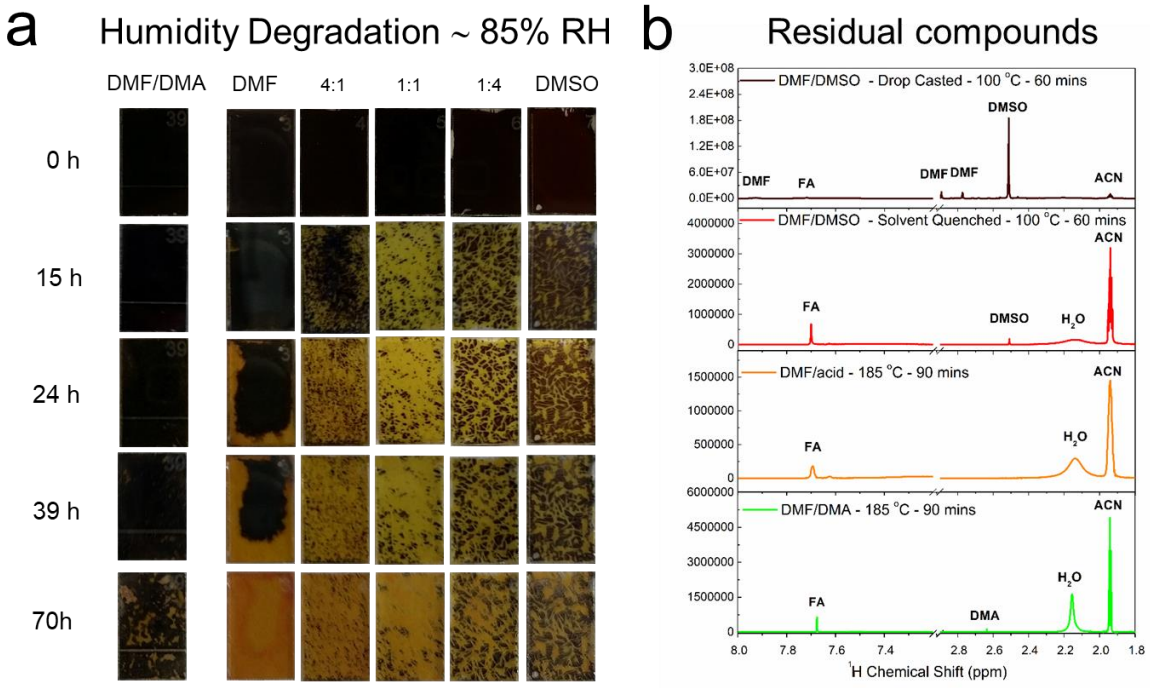

***Figure 4: Impact of solvent and fabrication method on* thin film humidity stability. A)** A series of photographs of thin films spin-coated fabricated with different ratios of DMF to DMSO, along with a comparison of the DMF/DMACl method. **B)** ^{1}H Nuclear Magnetic Resonance (NMR) spectra of perovskite thin films dispersed in acetonitrile-d_3 (CD_3CN). NMR spectra of a perovskite thin film prepared with a (Top) DMF/DMSO drop-casted method, (Middle) DMF/DMSO solvent-quenched method, and (Middle) DMF/Acid method, (Bottom) DMF/DMA method.

In Fig. 5, we show the thermal degradation of various perovskite films prepared with different deposition techniques when heated at 150 °C in a N_2 atmosphere.[45,83] We present in Fig. 5B-D the UV-Vis absorption spectra and the XRD pattern in Fig. 5E-G zoomed in the 11-15° 2θ region of the corresponding $FA_{0.83}Cs_{0.17}Pb(I_{0.8}Br_{0.2})_3$ perovskite films.

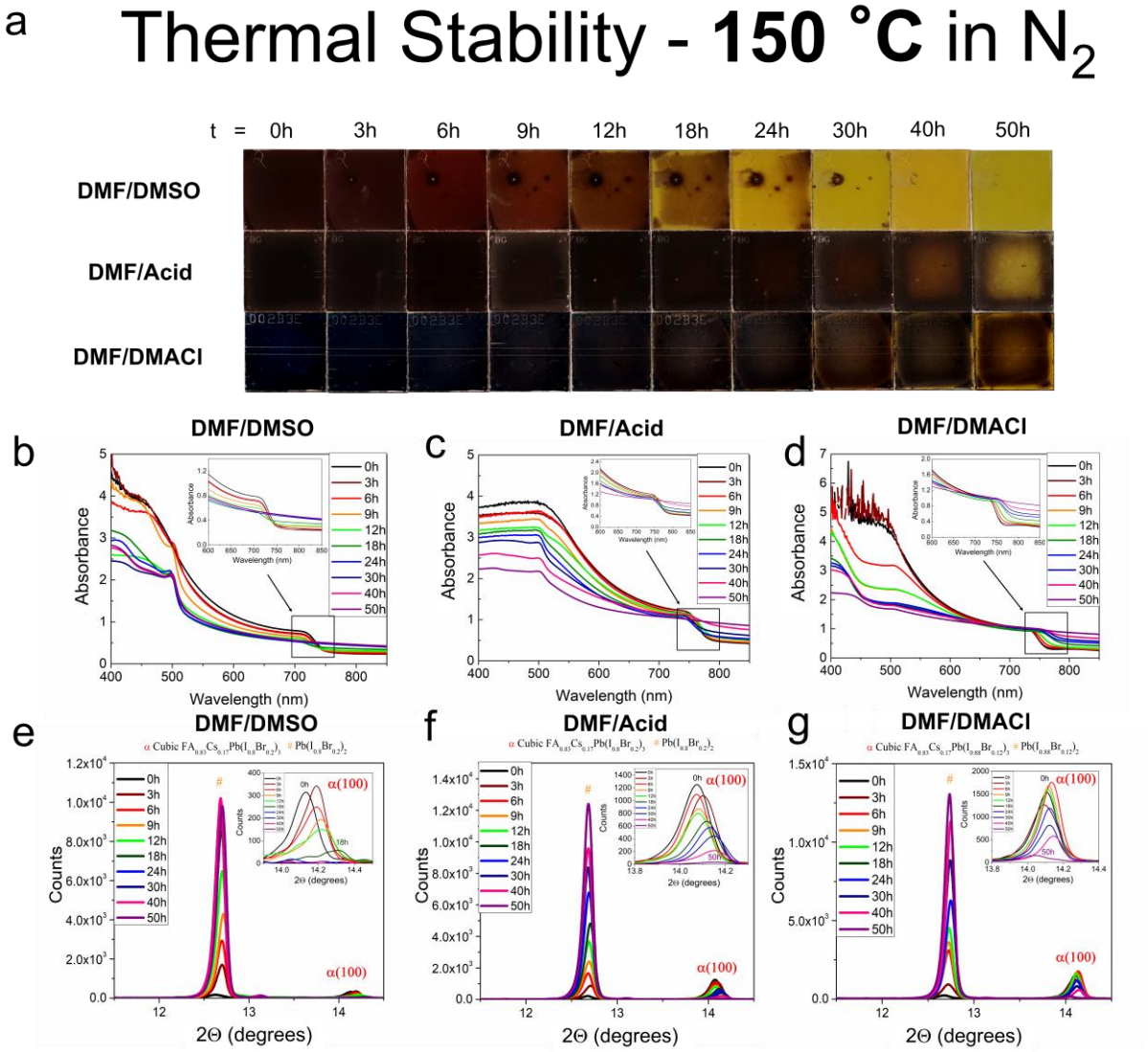

Figure 5: **Thin film thermal stability. a)** Photographs of perovskite thin films when heated at 150 °C in a N_2 atmosphere. The top row shows $FA_{0.83}Cs_{0.17}Pb(I_{0.8}Br_{0.2})_3$ films fabricated with the standard DMF/DMSO fabrication method, the middle row shows $FA_{0.83}Cs_{0.17}Pb(I_{0.8}Br_{0.2})_3$ films fabricated with the DMF/acid fabrication method, and the bottom row shows and $DMA_xFA_{0.83}Cs_{0.17}Pb(I_{0.8}Br_{0.2})_3Cl_x$ films fabricated with the DMF/DMACl fabrication method. **b, c, d)** Ultraviolet-visible (UV-Vis) absorbance spectra of films of corresponding films. **e, f, g)** XRD pattern of corresponding films, where # and α stand for the reflections originated from the PbX_2 (X is a mixture of I, Br and Cl) and cubic perovskite phase, respectively. The insets in **e, f, g)** show the enlarged XRD patterns highlighting the evolution of the cubic perovskite phase during the thermal stressing course.

The DMF/DMSO perovskite film shows a significantly faster rate of "yellowing", which occurred within the first 24 hours of 150 °C heating, compared to both DMF/acid or DMF/DMACl processed films, which remained dark until 50 h. We observed a similar behaviour for the wide bandgap $FA_{0.83}Cs_{0.17}Pb(I_{0.6}Br_{0.4})_3$ perovskite compositions (Supplementary Fig. 26). Neat $FAPbI_3$ or $CsPbI_3$ perovskite compositions are prone to revert

from their black perovskite phase to a yellow non-corner-sharing phase when cooled down to room temperature or exposed to moisture.[84–88] However, excess heat can also create a similar colour change, where thermal decomposition occurs when the more-volatile organic matter is removed from the crystal lattice when exposed to heat, creating a $Pb(Br_xI_{1-x})_2$ film associated with an XRD peak located at $2\theta \sim 12.7°$. In Fig. 5B, we observe that the DMF/DMSO processed perovskite films show a gradual decrease in the sharpness of the perovskite absorption onset and a complete disappearance of absorption onset after only 24 hours of heating at 150 °C. On the other hand, the DMF/acid and/or DMF/DMACl fabrication routes showed roughly half the degradation rate, where the perovskite absorption onset fully disappeared after 40-50 h. Similarly, we observe the complete loss of the perovskite (100) peak, located at $2\theta = \sim 14°$, after 18 hours of heating for the DMF/DMSO route and 50 hours for both the DMF/acid and DMF/DMACl route films. Correspondingly, we observe a rise of the $Pb(Br_xI_{1-x})_2$ peak located around $2\theta \approx 12.7°$. In Supplementary Fig. 27 we present the evolution of the normalised intensity ratio between lead halide and perovskite (100) XRD peak versus thermal aging time. To further assess and quantify the thermal stability of these films, we performed thermogravimetric analysis (TGA) directly on perovskite-coated glass substrates to account for the variation in morphology, topography, and crystal orientation of films produced via these different fabrication methods. In Supplementary Fig. 27, we show a 14 °C difference, from 265 to 279 °C, between the peaks of 1st derivative of DMF/DMSO and the DMF/acid films. Further details and results are provided in the supplementary information (Supplementary Fig. 28-30). Lastly, we conducted an in-situ thermal degradation XRD study of a series of films, with/without DMSO and/or DMACl, stressed at 130 °C in an air atmosphere with ~33% RH. (Supplementary Fig. 31).

To assess the performance of these different processed perovskite absorber layers in complete solar cells, we fabricated both negative-intrinsic-positive (n-i-p) and p-i-n device configurations. The device structures were FTO/SnO_2/perovskite/Spiro-OMeTAD/Au for the n-i-p cells and FTO/PTAA/Al_2O_3 nanoparticles/perovskite/LiBr/C_{70}/Zr(Acac)/PEIE/Au for the p-i-n cells. The devices fabricated via the DMF/DMACl route, reaching 18.8% (18.2% steady-state) PCE in an n-i-p configuration and 16.7% (16.1% stabilized) in a p-i-n architecture, which is comparable to the DMF/DMSO processed devices, which achieved 18.3% PCE (18.3% stabilized) in an n-i-p configuration and 16.2 % (14.8% stabilized) in the p-i-n configuration (Supplementary Fig. 32). By further optimizing the compact SnO_2 electron transport layer processed via chemical bath deposition and introducing a KCl treatment to this layer, we obtained a champion device for the DMF/DMACl n-i-p device, reaching PCE of 20.2% (JV) and 19.9% (steady-state) (Supplementary Fig. 33).

Although the n-i-p, spiro-OMeTAD-based devices tend to outperform the p-i-n in terms of PCE, their operational stability suffers due to HTM instabilities linked to hygroscopic and volatile dopants.[89–96] In order to assess the long-term stability of these two distinct crystallization routes in complete PV devices, we aged two populations of p-i-n devices (DMF/DMSO and DMF/DMACl) under simulated sunlight at 65 °C for over 2000 hours and a separate set of populations at 85 °C for over 1000 hours (Fig. 6A-E). We employed a glass/glass encapsulation technique, sealed under an N_2 atmosphere with a UV-cured epoxy resin.

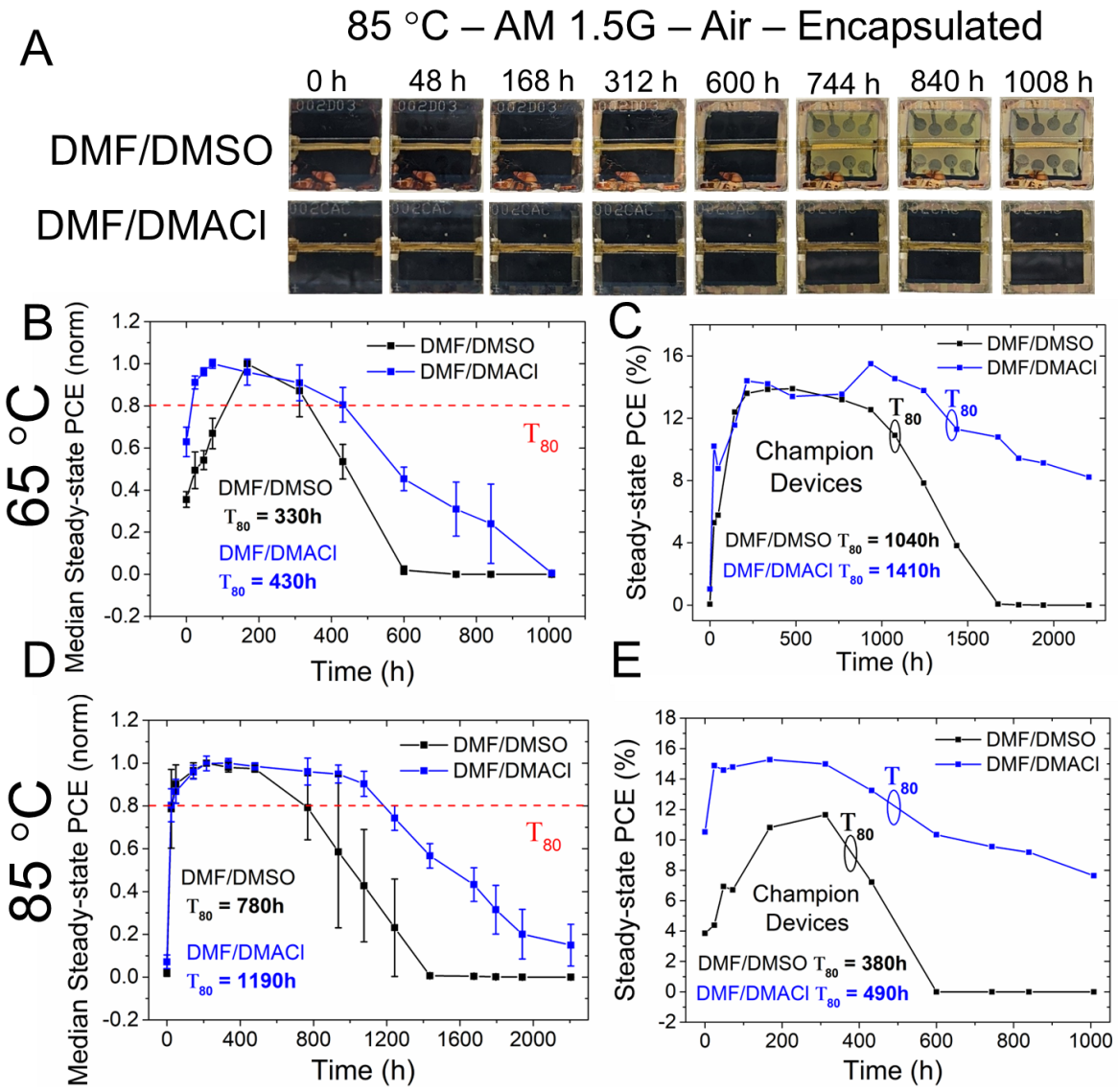

Figure 6: Stability comparison of perovskite solar cell devices prepared with DMF/DMSO or the DMF/DMACl fabrication method. *A) Photographs of encapsulated DMF/DMSO (control) and DMF/DMACl p-i-n devices taken at various aging times under full spectrum simulated AM 1.5, 76 mW cm^{-2} average irradiance at V_{OC} in air without a UV filter at 85 °C, using a Suntest XLS$^+$ aging box which irradiates pulsed light. B, C) Evolution of stabilized PCE, measured at its peak efficiency, between two statistical populations and champions devices of encapsulated devices of DMF/DMSO and DMF/DMACl designs aged under simulated sunlight at 65 °C. D, E) Evolution of steady-state PCE, measured at its peak efficiency, between two statistical populations and champions devices of encapsulated devices of DMF/DMSO and DMF/DMACl designs aged under simulated sunlight at 85 °C. The error bars were calculated using the median absolute deviation (MAD) as a measure of statistical dispersion.*

In contrast to the n-i-p cells, these p-i-n cells do not exhibit a sharp early degradation, known as the "burn-in" period.[13] In contrast, we see a significant gain in PCE over the first 200 hours of light and temperature exposure. We used this peak PCE to estimate the T_{80} lifetime of encapsulated cells, under full spectrum sunlight illumination, at 65 °C and open-circuit

conditions, resulting in a T_{80} lifetime of 1040 (780) hours for the champion (median) control DMF/DMSO device and 1410 (1190) hours for the champion (median) DMF/DMACl device.[13] Furthermore, for aging past 1600 hours, we observe that the control devices have all completely died, consistent with their bleached visual appearance (figure 6a, b and c), whereas the DMF/DMACl processed devices sustain on average 50% of their peak performance at 1600 hours, with the hero cell sustaining >70% of its peak performance at this time. We aged a sizeable device population of N=106 (JV) and N=32 (stabilised) devices to establish a statistical significance between these two designs (Fig. 5B-C and Supplementary Fig. 34). We also conducted the same full illumination degradation study at a higher temperature of 85 °C, where the DMF/DMSO devices obtained a champion (median) T_{80} of 380 (330) hours, while the DMF/DMACl devices obtained a champion (median) T_{80} of 490 (430) hours for a population size of N=72 (JV) and N=27 (stabilised) (Fig. 5D-E and Supplementary Fig. 35). Hence, the improved stability of the perovskite absorber layer processed via the DMF/DMACl route has resulted in a significant increase in the overall PV device stability under elevated temperature light soaking. Incidentally, from these results, we can estimate a thermal degradation "acceleration factor" of roughly 1.7-fold per 10 °C increment for these devices. This can be useful for comparing the relative stability of different materials and devices stressed at different temperatures and is close to the 2-fold acceleration in degradation per 10 °C increment, which is expected for the degradation of silicon PV cells.[97] We note here that we age our devices at open-circuit conditions, which is expected to accelerate the degradation compared to measuring it at the maximum power point.[98]

To summarise our findings concerning enhanced stability, we have identified chemically a directed pathway for controlling crystalization, the defect structure and crystal orientation of perovskite films, with commensurate changes in structure, morphology and crystallinity of the grains. This slow 2H to 3C crystallization sequence results in enhanced

materials properties, including thermal, moisture, and operational stability of devices employing these films. We postulate that the mechanism driving this increased stability is directly linked to the overall higher material quality defined by a significantly higher level of crystal order in the lattice, a stronger (100) preferred orientation, larger grain sizes, and fewer crystalline defects as inferred from reduced microstrain. Single crystals are known to retain their crystal structure for longer periods in comparison to polycrystalline thin films when exposed to humidity.[99,100] On the other hand, the hydration process is significantly faster for thin films due to their relatively high surface-to-volume ratio and the abundance of grain boundaries and surface defects.[100] It has been previously postulated and shown that grain boundaries (or the defects present at grain boundaries) offer a higher degree of adsorption and penetration of polar water molecules, allowing for the formation of hydrated perovskite phases.[101–103] Degradation is thought to proceed via surface defects due, for instance, to the adsorption of water or oxygen.[104] Thermal instability has also been linked to a disordered crystal structure, enhanced by lattice dislocations and defects along the surface of the grain boundaries.[100,105–107] These structural imperfections may increase the rate of decomposition by reducing the likelihood of forming a continuous lead halide plane, which can slow down, or "self-terminate" the decomposition. Hence, defect control via process or additives, as in this case, promotes a reduction in the density of surface defects, particularly those located at the grain boundaries. Thus, reducing the number of sites at which oxygen and water can adsorb to the perovskite surface and undergo chemical reactions with the ions in the perovskite is likely to lead to enhanced stability.

Conclusion:

In this work, we have presented a method of accurately controlling the precursor phase evolution involved from the 2H to 3C crystallization sequence of the $FA_yCs_{1-y}Pb(Br_xI_{1-x})_3$ perovskite system via the addition of DMACl. We show that dimethylammonium is produced in the precursor solution via the degradation of DMF in the presence of water and hydrohalic acids. The addition of DMA^+ allowed us to remove DMSO from the precursor solution, which is commonly used to form $DMSO{\cdot}PbI_2$ and $(DMSO)_2{\cdot}PbI_2$ complexes to control the 2H to 3C crystallization process. In turn, we avoid the possibility of residual DMSO in the film, potentially increasing its hygroscopicity or introducing defects. Furthermore, this slow crystallization process results in (100) preferred orientation and a high degree of crystallinity. This improved material quality led to higher overall perovskite stability on many forefronts, including thermal, humidity and light stability. In turn, we could achieve a champion T_{80} lifetime of 1410 hours at 65 °C and 490 hours at 85 °C, for encapsulated DMF/DMACl devices, under full spectrum sunlight illumination and open-circuit conditions. We expect future improvements to be achieved by a better understanding of the chemistry of intermediate phases and the mechanism by which they impact the crystallization kinetics and grain orientation of perovskite films. This insight may allow these intermediate phases to act as both key indicators and an avenue for improved process control of the perovskite defect structure for high stability. Thus, our findings elucidate a path to identifying and engineering highly stable perovskite absorber layers and represent an important step towards gaining full control of metal-halide perovskites thin films for other optoelectronic applications. We expect that applying additional defect-passivation to the surface of these films is likely to lead to even further improvements in stability and performance.

Acknowledgement

The research leading to these results has received funding from the European Union's Horizon 2020 research and innovation programme under grant agreement No. 763977 of the PerTPV project and the innovation programme under the Marie Skłodowska-Curie grant agreement No 764787. The authors acknowledge financial support from EPSRC (UK), grant EP/S004947/1. The authors also acknowledge the financial support from the Australian Research Council (ARC) Centre of Excellence in Exciton Science (ACEx:CE170100026). D.P.M. acknowledges financial support from the Australian Centre for Advanced Photovoltaics (ACAP), the Australian Renewable Energy Agency and the Marie Skłodowska-Curie grant agreement SAMA No 101029896. The work by S.P.H, and L.T.S was supported by the De-Risking Halide Perovskite Solar Cells program of the National Center for Photovoltaics, funded by the U.S. Department of Energy, Office of Energy Efficiency and Renewable Energy, Solar Energy Technologies Office under the U.S. Department of Energy under contract no. DE-AC36-08GO28308 with Alliance for Sustainable Energy, Limited Liability Company (LLC), the Manager and Operator of the National Renewable Energy Laboratory. Work by J. J. B was supported by the Office of Naval Research. The views expressed in the article do not necessarily represent the views of the DOE or the U.S. Government. We would like to acknowledge Prof. Fritz Vollrath and the Oxford Silk Group for their help and equipment. Use of the Stanford Synchrotron Radiation Lightsource, SLAC National Accelerator Laboratory, was supported by the U.S. Department of Energy, Office of Basic Energy Sciences under Contract No. DE-AC02-76SF00515. We would like also to acknowledge the Monash X-ray Platform (MXP).

References

[1] NREL National Renewable Energy Laboratory, “Best Research-Cell Efficiency Chart | Photovoltaic Research | NREL,” can be found under https://www.nrel.gov/pv/cell-efficiency.html, **2021**.

[2] A. Kojima, K. Teshima, Y. Shirai, T. Miyasaka, *J. Am. Chem. Soc.* **2009**, *131*, 6050.

[3] M. M. Lee, J. Teuscher, T. Miyasaka, T. N. Murakami, H. J. Snaith, *Science* **2012**, *338*, 643.

[4] D. B. Mitzi, S. Wang, C. A. Feild, C. A. Chess, A. M. Guloy, *Science* **1995**, *267*, 1473.

[5] M. Liu, M. B. Johnston, H. J. Snaith, *Nature* **2013**, *501*, 395.

[6] J. Burschka, N. Pellet, S.-J. Moon, R. Humphry-Baker, P. Gao, M. K. Nazeeruddin, M. Grätzel, *Nature* **2013**, *499*, 316.

[7] O. Malinkiewicz, A. Yella, Y. H. Lee, G. M. Espallargas, M. Graetzel, M. K. Nazeeruddin, H. J. Bolink, *Nat. Photonics* **2013**, *8*, 128.

[8] S. D. Stranks, G. E. Eperon, G. Grancini, C. Menelaou, M. J. P. Alcocer, T. Leijtens, L. M. Herz, A. Petrozza, H. J. Snaith, *Science* **2013**, *342*, 341.

[9] H.-S. Kim, C.-R. Lee, J.-H. Im, K.-B. Lee, T. Moehl, A. Marchioro, S.-J. Moon, R. Humphry-Baker, J.-H. Yum, J. E. Moser, M. Grätzel, N.-G. Park, *Sci. Rep.* **2012**, *2*, 591.

[10] J.-H. Im, C.-R. Lee, J.-W. Lee, S.-W. Park, N.-G. Park, *Nanoscale* **2011**, *3*, 4088.

[11] W. Ke, C. Xiao, C. Wang, B. Saparov, H.-S. Duan, D. Zhao, Z. Xiao, P. Schulz, S. P. Harvey, W. Liao, W. Meng, Y. Yu, A. J. Cimaroli, C.-S. Jiang, K. Zhu, M. Al-Jassim, G. Fang, D. B. Mitzi, Y. Yan, *Adv. Mater.* **2016**, *28*, 5214.

[12] T. Baikie, Y. Fang, J. M. Kadro, M. Schreyer, F. Wei, S. G. Mhaisalkar, M. Gratzel, T. J. White, *J. Mater. Chem. A* **2013**, *1*, 5628.

[13] M. V. Khenkin, E. A. Katz, A. Abate, G. Bardizza, J. J. Berry, C. Brabec, F. Brunetti, V. Bulović, Q. Burlingame, A. Di Carlo, R. Cheacharoen, Y.-B. Cheng, A. Colsmann, S. Cros, K. Domanski, M. Dusza, C. J. Fell, S. R. Forrest, Y. Galagan, D. Di Girolamo, M. Grätzel, A. Hagfeldt, E. von Hauff, H. Hoppe, J. Kettle, H. Köbler, M. S. Leite, S. Liu, Y.-L. Loo, J. M. Luther, C.-Q. Ma, M. Madsen, M. Manceau, M. Matheron, M. McGehee, R. Meitzner, M. K. Nazeeruddin, A. F. Nogueira, Ç. Odabaşı, A. Osherov, N.-G. Park, M. O. Reese, F. De Rossi, M. Saliba, U. S. Schubert, H. J. Snaith, S. D. Stranks, W. Tress, P. A. Troshin, V. Turkovic, S. Veenstra, I. Visoly-Fisher, A. Walsh, T. Watson, H. Xie, R. Yıldırım, S. M. Zakeeruddin, K. Zhu, M. Lira-Cantu, *Nat. Energy* **2020**, *5*, 35.

[14] H. J. Snaith, P. Hacke, *Nat. Energy* **2018**, *3*, 459.

[15] J. A. Christians, S. N. Habisreutinger, J. J. Berry, J. M. Luther, *ACS Energy Lett.* **2018**, *3*, 2136.

[16] A. Hadipour, B. de Boer, P. W. M. Blom, *Org. Electron.* **2008**, *9*, 617.

[17] P. Holzhey, M. Saliba, *J. Mater. Chem. A* **2018**, *6*, 21794.

[18] L. Shi, M. P. Bucknall, T. L. Young, M. Zhang, L. Hu, J. Bing, D. S. Lee, J. Kim, T. Wu, N. Takamure, D. R. McKenzie, S. Huang, M. A. Green, A. W. Y. Ho-Baillie, *Science* **2020**, *368*, DOI 10.1126/science.aba2412.

[19] R. Cheacharoen, N. Rolston, D. Harwood, K. A. Bush, R. H. Dauskardt, M. D. McGehee, *Energy Environ. Sci.* **2018**, *11*, 144.

[20] L. Xie, J. Chen, P. Vashishtha, X. Zhao, G. S. Shin, S. G. Mhaisalkar, N. G. Park, *ACS Energy Lett.* **2019**, *4*, 2192.

[21] M. Stolterfoht, C. M. Wolff, J. A. Márquez, S. Zhang, C. J. Hages, D. Rothhardt, S. Albrecht, P. L. Burn, P. Meredith, T. Unold, D. Neher, *Nat. Energy* **2018**, *3*, 847.

[22] C. M. Wolff, L. Canil, C. Rehermann, N. Ngoc Linh, F. Zu, M. Ralaiarisoa, P. Caprioglio, L. Fiedler, M. Stolterfoht, S. Kogikoski, I. Bald, N. Koch, E. L. Unger, T. Dittrich, A. Abate, D. Neher, *ACS Nano* **2020**, *14*, 1445.

[23] Y. Hou, X. Du, S. Scheiner, D. P. McMeekin, Z. Wang, N. Li, M. S. Killian, H. Chen, M. Richter, I. Levchuk, N. Schrenker, E. Spiecker, T. Stubhan, N. A. Luechinger, A. Hirsch, P. Schmuki, H. P. Steinrück, R. H. Fink, M. Halik, H. J. Snaith, C. J. Brabec, *Science* **2017**, *358*, 1192.

[24] J. A. Christians, P. Schulz, J. S. Tinkham, T. H. Schloemer, S. P. Harvey, B. J. Tremolet de Villers, A. Sellinger, J. J. Berry, J. M. Luther, *Nat. Energy* **2018**, *3*, 68.

[25] S. Bai, P. Da, C. Li, Z. Wang, Z. Yuan, F. Fu, M. Kawecki, X. Liu, N. Sakai, J. T. W. Wang, S. Huettner, S. Buecheler, M. Fahlman, F. Gao, H. J. Snaith, *Nature* **2019**, *571*, 245.

[26] Y.-H. Lin, N. Sakai, P. Da, J. Wu, H. C. Sansom, A. J. Ramadan, S. Mahesh, J. Liu, R. D. J. Oliver, J. Lim, L. Aspitarte, K. Sharma, P. K. Madhu, A. B. Morales-Vilches, P. K. Nayak, S. Bai, F. Gao, C. R. M. Grovenor, M. B. Johnston, J. G. Labram, J. R. Durrant, J. M. Ball, B. Wenger, B. Stannowski, H. J. Snaith, *Science* **2020**, *369*, 96.

[27] S. Wang, A. Wang, X. Deng, L. Xie, A. Xiao, C. Li, Y. Xiang, T. Li, L. Ding, F. Hao, *J. Mater. Chem. A* **2020**, *8*, 12201.

[28] M. Qin, J. Cao, T. Zhang, J. Mai, T. K. Lau, S. Zhou, Y. Zhou, J. Wang, Y. J. Hsu, N. Zhao, J. Xu, X. Zhan, X. Lu, *Adv. Energy Mater.* **2018**, *8*, 1703399.

[29] D. P. McMeekin, G. Sadoughi, W. Rehman, G. E. Eperon, M. Saliba, M. T. Horantner, A. Haghighirad, N. Sakai, L. Korte, B. Rech, M. B. Johnston, L. M. Herz, H. J. Snaith, *Science* **2016**, *351*, 151.

[30] M. Saliba, T. Matsui, J.-Y. Seo, K. Domanski, J.-P. Correa-Baena, N. Mohammad K., S. M. Zakeeruddin, W. Tress, A. Abate, A. Hagfeldt, M. Grätzel, *Energy Environ. Sci.* **2016**, DOI 10.1039/C5EE03874J.

[31] J.-W. Lee, D.-H. Kim, H.-S. Kim, S.-W. Seo, S. M. Cho, N.-G. Park, *Adv. Energy Mater.* **2015**, *5*, 1501310.

[32] N. Pellet, P. Gao, G. Gregori, T.-Y. Yang, M. K. Nazeeruddin, J. Maier, M. Grätzel, *Angew. Chem. Int. Ed. Engl.* **2014**, *53*, 3151.

[33] C. Yi, J. Luo, S. Meloni, A. Boziki, N. Ashari-Astani, C. Grätzel, S. M. Zakeeruddin, U. Rothlisberger, M. Grätzel, *Energy Environ. Sci.* **2015**, *9*, 656.

[34] Z. Li, M. Yang, J.-S. Park, S.-H. Wei, J. J. Berry, K. Zhu, *Chem. Mater.* **2016**, *28*, 284.

[35] N. J. Jeon, J. H. Noh, Y. C. Kim, W. S. Yang, S. Ryu, S. Il Seok, *Nat. Mater.* **2014**, *13*, 897.

[36] M. Xiao, F. Huang, W. Huang, Y. Dkhissi, Y. Zhu, J. Etheridge, A. Gray-Weale, U. Bach, Y. B. Cheng, L. Spiccia, *Angew. Chemie - Int. Ed.* **2014**, *53*, 9898.

[37] Y. Rong, S. Venkatesan, R. Guo, Y. Wang, J. Bao, W. Li, Z. Fan, Y. Yao, *Nanoscale* **2016**, *8*, 12892.

[38] W. S. Yang, J. H. Noh, N. J. Jeon, Y. C. Kim, S. Ryu, J. Seo, S. I. Seok, *Science* **2015**, *348*, 1234.

[39] J. Lee, S. Baik, *RSC Adv.* **2018**, *8*, 1005.

[40] S. J. Lee, J. H. Heo, S. H. Im, *ACS Appl. Mater. Interfaces* **2020**, *12*, 8233.

[41] A. Mutlu, T. Yeşil, D. Kiymaz, C. Zafer, *ACS Appl. Energy Mater.* **2021**, *4*, 47.

[42] D. Shi, V. Adinolfi, R. Comin, M. Yuan, E. Alarousu, A. Buin, Y. Chen, S. Hoogland, A. Rothenberger, K. Katsiev, Y. Losovyj, X. Zhang, P. A. Dowben, O. F. Mohammed, E. H. Sargent, O. M. Bakr, *Science* **2015**, *347*, 519.

[43] Q. Dong, Y. Fang, Y. Shao, P. Mulligan, J. Qiu, L. Cao, J. Huang, *Science* **2015**, *347*, 967.

[44] M. I. Saidaminov, V. Adinolfi, R. Comin, A. L. Abdelhady, W. Peng, I. Dursun, M. Yuan, S. Hoogland, E. H. Sargent, O. M. Bakr, *Nat. Commun.* **2015**, *6*, 8724.

[45] Q. Wang, B. Chen, Y. Liu, Y. Deng, Y. Bai, Q. Dong, J. Huang, *Energy Environ. Sci.* **2017**, *10*, 516.

[46] N. K. Noel, M. Congiu, A. J. Ramadan, S. Fearn, D. P. McMeekin, J. B. Patel, M. B. Johnston, B. Wenger, H. J. Snaith, *Joule* **2017**, *1*, 328.

[47] B. Dou, L. M. Wheeler, J. A. Christians, D. T. Moore, S. P. Harvey, J. J. Berry, F. S. Barnes, S. E. Shaheen, M. F. A. M. van Hest, *ACS Energy Lett.* **2018**, *3*, 979.

[48] W. Ke, I. Spanopoulos, C. C. Stoumpos, M. G. Kanatzidis, *Nat. Commun.* **2018**, *9*, 1.

[49] A. R. Marshall, H. C. Sansom, M. M. McCarthy, J. H. Warby, O. J. Ashton, B. Wenger, H. J. Snaith, *Sol. RRL* **2021**, *5*, 2000599.

[50] D. P. McMeekin, Z. Wang, W. Rehman, F. Pulvirenti, J. B. Patel, N. K. Noel, M. B. Johnston, S. R. Marder, L. M. Herz, H. J. Snaith, *Adv. Mater.* **2017**, *29*, DOI 10.1002/adma.201607039.

[51] N. K. Noel, M. Congiu, A. J. Ramadan, S. Fearn, D. P. McMeekin, J. B. Patel, M. B. Johnston, B. Wenger, H. J. Snaith, *Joule* **2017**, *1*, DOI 10.1016/j.joule.2017.09.009.

[52] K. Yan, M. Long, T. Zhang, Z. Wei, H. Chen, S. Yang, J. Xu, *J. Am. Chem. Soc.* **2015**, *137*, 4460.

[53] J. K. Magtaan, M. Devocelle, F. Kelleher, *J. Pept. Sci.* **2019**, *25*, e3139.

[54] M. T. Hörantner, H. Snaith, *Energy Environ. Sci.* **2017**, *10*, 1983.

[55] K. A. Bush, A. F. Palmstrom, Z. J. Yu, M. Boccard, R. Cheacharoen, J. P. Mailoa, D. P. McMeekin, R. L. Z. Hoye, C. D. Bailie, T. Leijtens, I. M. Peters, M. C. Minichetti, N. Rolston, R. Prasanna, S. Sofia, D. Harwood, W. Ma, F. Moghadam, H. J. Snaith, T. Buonassisi, Z. C. Holman, S. F. Bent, M. D. McGehee, *Nat. Energy* **2017**, *2*, DOI 10.1038/nenergy.2017.9.

[56] M. T. Horantner, P. K. Nayak, S. Mukhopadhyay, K. Wojciechowski, C. Beck, D. McMeekin, B. Kamino, G. E. Eperon, H. J. Snaith, *Adv. Mater. Interfaces* **2016**, *3*, 1500837.

[57] G. E. Eperon, T. Leijtens, K. A. Bush, R. Prasanna, T. Green, J. T.-W. Wang, D. P. McMeekin, G. Volonakis, R. L. Milot, R. May, A. Palmstrom, D. J. Slotcavage, R. A. Belisle, J. B. Patel, E. S. Parrott, R. J. Sutton, W. Ma, F. Moghadam, B. Conings, A. Babayigit, H.-G. Boyen, S. Bent, F. Giustino, L. M. Herz, M. B. Johnston, M. D. McGehee, H. J. Snaith, *Science* **2016**, *354*, DOI 10.1126/science.aaf9717.

[58] A. J. Barker, A. Sadhanala, F. Deschler, M. Gandini, S. P. Senanayak, P. M. Pearce, E. Mosconi, A. Pearson, Y. Wu, A. R. Srimath Kandada, T. Leitjens, F. De Angelis, S. E. Dutton, A. Petrozza, R. H. Friend, *ACS Energy Lett.* **2017**, *2*, 1416.

[59] E. T. Hoke, D. J. Slotcavage, E. R. Dohner, A. R. Bowring, H. I. Karunadasa, M. D. McGehee, *Chem. Sci.* **2014**, *6*, 613.

[60] S. Mahesh, J. M. Ball, R. D. J. Oliver, D. P. McMeekin, P. K. Nayak, M. B. Johnston, H. J. Snaith, *Energy Environ. Sci.* **2020**, *13*, 258.

[61] F. Penã-Camargo, P. Caprioglio, F. Zu, E. Gutierrez-Partida, C. M. Wolff, K. Brinkmann, S. Albrecht, T. Riedl, N. Koch, D. Neher, M. Stolterfoht, *ACS Energy Lett.* **2020**, *5*, 2728.

[62] E. Centurioni, *Appl. Opt.* **2005**, *44*, 7532.

[63] W. Rehman, D. P. McMeekin, J. B. Patel, R. L. Milot, M. B. Johnston, H. J. Snaith, L. M. Herz, *Energy Environ. Sci.* **2017**, *10*, 361.

[64] J. M. Ball, A. Petrozza, *Nat. Energy* **2016**, *1*, 1.

[65] A. J. Knight, J. B. Patel, H. J. Snaith, M. B. Johnston, L. M. Herz, *Adv. Energy Mater.* **2020**, *10*, 1903488.

[66] S. G. Motti, J. B. Patel, R. D. J. Oliver, H. J. Snaith, M. B. Johnston, L. M. Herz, *Nat. Commun. 2021 121* **2021**, *12*, 1.

[67] M. Kim, G. H. Kim, T. K. Lee, I. W. Choi, H. W. Choi, Y. Jo, Y. J. Yoon, J. W. Kim, J. Lee, D. Huh, H. Lee, S. K. Kwak, J. Y. Kim, D. S. Kim, *Joule* **2019**, *3*, 2179.

[68] C. C. Stoumpos, L. Mao, C. D. Malliakas, M. G. Kanatzidis, *Inorg. Chem.* **2017**, *56*, 56.

[69] N. V. Tarakina, A. P. Tyutyunnik, G. V. Bazuev, A. D. Vasilev, C. Gould, I. V. Nikolaenko, I. F. Berger, *Dalt. Trans.* **2015**, *44*, 18527.

[70] P. Gratia, I. Zimmermann, P. Schouwink, J. H. Yum, J. N. Audinot, K. Sivula, T. Wirtz, M. K. Nazeeruddin, *ACS Energy Lett.* **2017**, *2*, 2686.

[71] J. Tian, D. B. Cordes, C. Quarti, D. Beljonne, A. M. Z. Slawin, E. Zysman-Colman, F. D. Morrison, *ACS Appl. Energy Mater.* **2019**, *2*, 5427.

[72] A. Mancini, P. Quadrelli, G. Amoroso, C. Milanese, M. Boiocchi, A. Sironi, M. Patrini, G. Guizzetti, L. Malavasi, *J. Solid State Chem.* **2016**, *240*, 55.

[73] A. García-Fernández, E. J. Juarez-Perez, J. M. Bermúdez-García, A. L. Llamas-Saiz, R. Artiaga, J. J. López-Beceiro, M. A. Señarís-Rodríguez, M. Sánchez-Andújar, S. Castro-García, *J. Mater. Chem. C* **2019**, *7*, 10008.

[74] A. García-Fernández, J. M. Bermúdez-García, S. Castro-García, A. L. Llamas-Saiz, R. Artiaga, J. López-Beceiro, S. Hu, W. Ren, A. Stroppa, M. Sánchez-Andújar, M. A. Señarís-Rodríguez, *Inorg. Chem.* **2017**, *56*, 4918.

[75] D. T. Moore, H. Sai, K. W. Tan, D. M. Smilgies, W. Zhang, H. J. Snaith, U. Wiesner, L. A. Estroff, *J. Am. Chem. Soc.* **2015**, *137*, 2350.

[76] G. E. Eperon, K. H. Stone, L. E. Mundt, T. H. Schloemer, S. N. Habisreutinger, S. P. Dunfield, L. T. Schelhas, J. J. Berry, D. T. Moore, G. E. Eperon, D. T. Moore, *ACS Energy Lett.* **2020**, *5*, 1856.

[77] C. Gehrmann, D. A. Egger, *Nat. Commun.* **2019**, *10*, 1.

[78] L. Oesinghaus, J. Schlipf, N. Giesbrecht, L. Song, Y. Hu, T. Bein, P. Docampo, P. Müller-Buschbaum, *Adv. Mater. Interfaces* **2016**, *3*, 1600403.

[79] H. Chen, X. Ding, P. Xu, T. Hayat, A. Alsaedi, J. Yao, Y. Ding, S. Dai, *ACS Appl. Mater. Interfaces* **2018**, *10*, 1781.

[80] N. Ahn, D. Y. Son, I. H. Jang, S. M. Kang, M. Choi, N. G. Park, *J. Am. Chem. Soc.* **2015**, *137*, 8696.

[81] Y. Rong, Z. Tang, Y. Zhao, X. Zhong, S. Venkatesan, H. Graham, M. Patton, Y. Jing, A. M. Guloy, Y. Yao, *Nanoscale* **2015**, *7*, 10595.

[82] G. R. Fulmer, A. J. M. Miller, N. H. Sherden, H. E. Gottlieb, A. Nudelman, B. M. Stoltz, J. E. Bercaw, K. I. Goldberg, *Organometallics* **2010**, *29*, 2176.

[83] C.-H. Chiang, C.-G. Wu, *ChemSusChem* **2016**, *9*, 2666.

[84] G. E. Eperon, G. M. Paternò, R. J. Sutton, A. Zampetti, A. A. Haghighirad, F. Cacialli, H. J. Snaith, *J. Mater. Chem. A* **2015**, *3*, 19688.

[85] T. Chen, B. J. Foley, C. Park, C. M. Brown, L. W. Harriger, J. Lee, J. Ruff, M. Yoon, J. J. Choi, S. H. Lee, *Sci. Adv.* **2016**, *2*, e1601650.

[86] R. J. Sutton, M. R. Filip, A. A. Haghighirad, N. Sakai, B. Wenger, F. Giustino, H. J. Snaith, *ACS Energy Lett.* **2018**, *3*, 1787.

[87] C. C. Stoumpos, L. Mao, C. D. Malliakas, M. G. Kanatzidis, *Inorg. Chem.* **2017**, *56*, 56.

[88] D. B. Straus, S. Guo, R. J. Cava, **2019**, DOI 10.1021/jacs.9b06055.

[89] B. Tan, S. R. Raga, A. S. R. Chesman, S. O. Fürer, F. Zheng, D. P. McMeekin, L. Jiang, W. Mao, X. Lin, X. Wen, J. Lu, Y. Cheng, U. Bach, *Adv. Energy Mater.* **2019**, 1901519.

[90] M. Hu, X. Wu, W. L. Tan, B. Tan, A. D. Scully, L. Ding, C. Zhou, Y. Xiong, F. Huang, A. N. Simonov, U. Bach, Y. B. Cheng, S. Wang, J. Lu, *ACS Appl. Mater. Interfaces* **2020**, *12*, 8260.

[91] T. H. Schloemer, J. A. Christians, J. M. Luther, A. Sellinger, *Chem. Sci.* **2019**, *10*, 1904.

[92] A. Pellaroque, N. K. Noel, S. N. Habisreutinger, Y. Zhang, S. Barlow, S. R. Marder, H. J. Snaith, *ACS Energy Lett.* **2017**, *2*, 2044.

[93] S. N. Habisreutinger, T. Leijtens, G. E. Eperon, S. D. Stranks, R. J. Nicholas, H. J. Snaith, *Nano Lett.* **2014**, *14*, 5561.

[94] W. H. Nguyen, C. D. Bailie, E. L. Unger, M. D. McGehee, *J. Am. Chem. Soc.* **2014**, *136*, 10996.

[95] A. K. Jena, M. Ikegami, T. Miyasaka, *ACS Energy Lett.* **2017**, *2*, 1760.

[96] S. Wang, M. Sina, P. Parikh, T. Uekert, B. Shahbazian, A. Devaraj, Y. S. Meng, *Nano Lett.* **2016**, *16*, 5594.

[97] H. J. Snaith, P. Hacke, *Nat. Energy* **2018**, *3*, 459.

[98] P. Holzhey, P. Yadav, S. H. Turren-Cruz, A. Ummadisingu, M. Grätzel, A. Hagfeldt, M. Saliba, *Mater. Today* **2019**, *29*, 10.

[99] J. Huang, Y. Shao, Q. Dong, *J. Phys. Chem. Lett.* **2015**, *6*, 3218.

[100] J. S. Manser, M. I. Saidaminov, J. A. Christians, O. M. Bakr, P. V. Kamat, *Acc. Chem. Res.* **2016**, *49*, 330.

[101] F. Hao, C. C. Stoumpos, Z. Liu, R. P. H. Chang, M. G. Kanatzidis, *J. Am. Chem. Soc.* **2014**, *136*, 16411.

[102] B. R. Vincent, K. N. Robertson, T. S. Cameron, O. Knop, *Can. J. Chem.* **1987**, *65*, 1042.

[103] A. M. A. Leguy, Y. Hu, M. Campoy-Quiles, M. I. Alonso, O. J. Weber, P. Azarhoosh,

M. van Schilfgaarde, M. T. Weller, T. Bein, J. Nelson, P. Docampo, P. R. F. Barnes, *Chem. Mater.* **2015**, *27*, 3397.

[104] Q. Sun, P. Fassl, D. Becker-Koch, A. Bausch, B. Rivkin, S. Bai, P. E. Hopkinson, H. J. Snaith, Y. Vaynzof, *Adv. Energy Mater.* **2017**, *7*, 1700977.

[105] S. Macpherson, T. A. S. Doherty, A. J. Winchester, S. Kosar, D. N. Johnstone, Y.-H. Chiang, K. Galkowski, M. Anaya, K. Frohna, A. N. Iqbal, S. Nagane, B. Roose, Z. Andaji-Garmaroudi, K. W. P. Orr, J. E. Parker, P. A. Midgley, K. M. Dani, S. D. Stranks, *Nat. 2022* **2022**, 1.

[106] G. Stokkan, S. Riepe, O. Lohne, W. Warta, *J. Appl. Phys.* **2007**, *101*, 053515.

[107] K. Hartman, M. Bertoni, J. Serdy, T. Buonassisi, *Appl. Phys. Lett.* **2008**, *93*, 122108.